Comparison of wavefront control algorithms and first results on the high-contrast imager for complex aperture telescopes (hicat) testbed

Lucie Leboulleux, Mamadou N'Diaye, A J Eldorado Riggs, Johan Mazoyer, Laurent Pueyo, Marshall Perrin, Sylvain Egron, Elodie Choquet, Jean-François Sauvage, Thierry Fusco, et al.

To cite this version:

Lucie Leboulleux, Mamadou N'Diaye, A J Eldorado Riggs, Johan Mazoyer, Laurent Pueyo, et al.. Comparison of wavefront control algorithms and first results on the high-contrast imager for complex aperture telescopes (hicat) testbed. International Conference on Space Optics - ICSO 2016,, Sep 2017, Biarritz, France. 10.1117/12.2296154 . hal-04023421

HAL Id: hal-04023421
https://hal.science/hal-04023421v1

PERFORMANCE STUDY ON SIMULATION MODE FOR WAVEFRONT CONTROL IN PRESENCE OF VIBRATION AND FIRST RESULTS ON THE HIGH-CONTRAST IMAGER FOR COMPLEX APERTURE TELESCOPES (HICAT) TESTBED

L. Leboulleux[1,2,3], M. N'Diaye[3], A. J. Eldorado Riggs[4], J. Mazoyer[3], L. Pueyo[3], M. Perrin[3], S. Egron[1,2,3], E. Choquet[4,5], J.-F. Sauvage[1], T. Fusco[2], R. Soummer[2]. Contact: lucie.leboulleux@lam.fr.
[1] ONERA, 29 Avenue de la Division Leclerc, 92320 Châtillon, France. [2] Aix Marseille Université, CNRS, LAM (Laboratoire d'Astrophysique de Marseille) UMR 7326, 13388, Marseille, France. [3] Space Telescope Science Institute, 3700 San Martin Drive, Baltimore, MD 21218, USA. [4] Jet Propulsion Laboratory, California Institute of Technology, 4800 Oak Grove Drive, MS 169-506, Pasadena, CA 91109, USA. [5]Hubble Fellow.

I. INTRODUCTION:

The next generation of space telescopes for direct imaging and spectroscopy of exoplanets includes telescopes with a monolithic mirror, such as the Wide Field Infrared Survey Telescope (WFIRST) [1] and Large Ultra-Violet Optical Infrared (LUVOIR) telescopes with segmented primary mirror, like ATLAST [2, 3] or HDST [4]. Because of the complexity of their pupils, high-contrast imaging becomes more challenging. Furthermore, space telescopes have huge requirements in term of contrast stability in the presence of vibrations.

The High-contrast imager for Complex Aperture Telescopes (HiCAT) testbed has been developed to enable studies on different components of high-contrast imaging, meaning starlight suppression, wavefront sensing (WFS), and wavefront control (WFC) for such unfriendly pupils. New coronagraph designs are currently developed on simulation [5, 6, 7] for a next implementation on the testbed. They will be complemented by two deformable mirrors (DM) pupil-remapping techniques (e.g. Active Control of Aperture Discontinuities [ACAD] [8, 9, 10]), that convert complex pupils into friendly apertures for coronagraphy.

In this communication, in section II we introduce the HiCAT testbed, focusing on its objectives and in particular the studies it will enable and the requirements that were deduced from these goals. These requirements lead to a final design and environment, that we also present here, before describing its current status.

In section III, we present the results of our simulations on wavefront control using a single DM and a classical Lyot coronagraph, including instability effects.

II. HICAT TESTBED:

The HiCAT testbed is currently being developed at the Space Telescope Science Institute (STScI), more precisely at the Russel B. Makidon Laboratory. This facility is dedicated to developing technologies for future space missions. In particular, HiCAT is designed to provide an integrated solution for high-contrast imaging for unfriendly aperture geometries. In the section, we will describe the objectives of this optical bench, its final optical and opto-mechanical design that was deduced from these requirements, the environment constraints, and finally the current status of the project.

A. Goals of the testbed

The HiCAT tesbed was designed to develop methods for high-contrast imaging, including a starlight and diffraction suppression system and wavefront sensing and control tools. These techniques have to be applied in complex-aperture case telescopes, which includes segment gaps, spiders and central obstruction.

Its initial contrast goal in air is 10^{-7} in a dark hole limited by $3\lambda/D$ and $10\lambda/D$ (where λ is the wavelength and D is the aperture diameter) in a 2% bandpass, in the visible, assuming a single Boston Micromachines-deformable mirror (DM), which should be improved to higher contrast after implementation of wavefront control methods.

To reach this contrast ratio, the testbed is designed to minimize the impact of its optical components on its final contrast, with focus on the sources of amplitude-induced errors from the propagation of out-of-pupil surfaces. To limit that effect, known as the Talbot effect, we place a requirement on the contrast contribution of amplitude errors to be one order of magnitude fainter than the total contrast, i.e. 10^{-8}. The goal is that, by minimizing the amplitude-induced errors due to the Talbot effect, the majority of the amplitude errors comes from the discontinuities in the pupil, such as the segment gaps, the spiders or the central obstruction and will be corrected using wavefront control and wavefront shaping.

Since HiCAT was designed to compensate for both amplitude errors due to its complex entrance pupil and phase errors due to surface errors and non-homogeneous reflectivities of the optical components, two Boston-DM are planned to be used. This is why this value of contrast should be then really improved after setting up the second DM in the optical path.

Such a contrast floor is below enough our contrast objective that the requirements will be achieved even in presence of complex aperture (central obstruction, spiders and segments) and in large spectral broadband operations.

But HiCAT also includes a coronagraph for starlight and diffraction-effect suppression, which is designed considering the contrast as a metric to optimize.

B. Optical and opto-mechanical design

The HiCAT testbed is designed to achieve these goals, performing high-contrast imaging in the case of unfriendly apertures. Therefore, it combines studies in coronagraphy, wavefront sensing and wavefront control, plus a simulated telescope with a complex pupil. The final layout is presented in Fig.1 and is explained in details in [7, 11, 12]. It is a purely reflective testbed, except for the last imaging lenses.

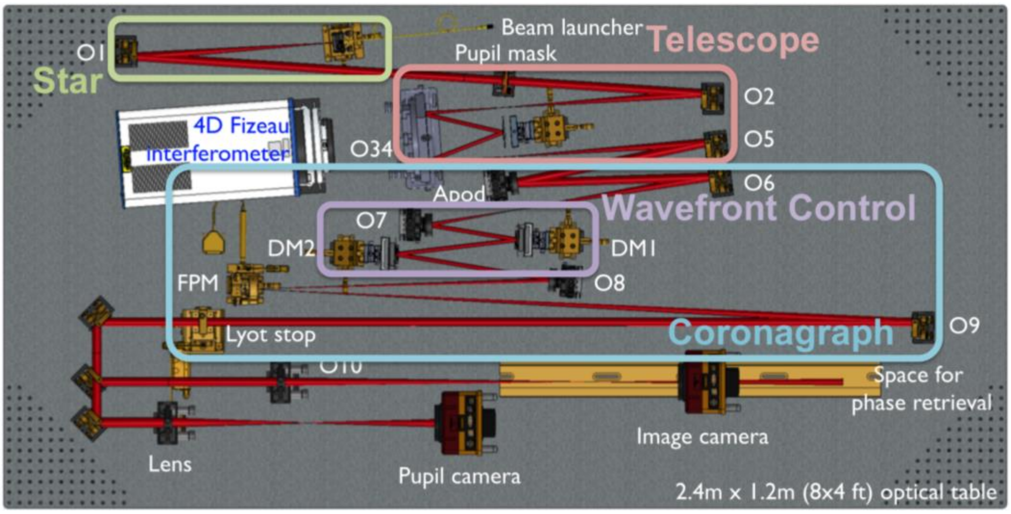

Fig. 1. HiCAT testbed design done with the software Solidworks, the beam is exported from Zemax. The telescope is simulated by a pupil mask, the segmented mirror and off-axis parabolas. The segmented mirror is conjugated with the pupil mask to form a segmented pupil with central obstruction and spider struts. The off-axis parabolas set the telescope aperture. The wavefront control is done with two deformable mirrors. The coronagraph is composed of an apodizer, a focal plane mask and a Lyot stop.

The telescope is simulated using:

- A non-circular entrance pupil mask with central obstruction and spiders to define an aperture shape. Its size is set the 20mm to enable small details to be represented (such as the spider) and the use of 1inch optics.
- A 37-segment Iris-AO MEMs deformable mirror with hexagonal segments that can be controlled in tip, tilt, and piston. The gaps between segments are between 10 and 12µm. This component is conjugated to the entrance pupil mask.

Together, these two components provide a segmented pupil similar to ATLAST. The segmented mirror can also be replaced with a high-quality flat mirror to give the possibility of studying AFTA-like pupils.

The chosen coronagraph is a Apodized Pupil Lyot Coronagraph (APLC), which combines a classical Lyot coronagraph with entrance pupil apodization [8, 9, 10] and that is currently implemented in the exoplanet direct imagers P1640, GPI, and SPHERE. It is then composed of:

- An apodizer, located in a pupil plane, so conjugated with the two optical components previously presented.
- A reflective focal plane mask (FPM), with a 334µm diameter central hole. The beam focal ratio at its location is set at F/80.
- A Lyot Stop, with a diameter equal to the entrance pupil.

Both the FPM and the Lyot Stop are motorized and can be controlled from a computer.

The final design of the apodizer is still under development, and the testbed is currently equipped with a Lyot coronagraph, the apodizer being replaced by a high-quality mirror. For more details about the investigations on coronagraph designs, please see [7]. Furthermore, thanks to the hole in the FPM, part of the beam can be reused and this coronagraph is compatible with a low-order wavefront sensor [13, 14, 15].

Finally, the wavefront sensing and control system includes:

- Two Boston Micromachines deformable mirrors (kilo-DM), which shows 952 actuators in a 9.9mm diameter disk. One of them is calibrated and set in a pupil plane [7], and the second one, currently replaced by a flat mirror, is located out of pupil. It will enable active correction for aperture discontinuities (ACAD) and both amplitude and phase control.
- A focal plane camera (CamF), with a motorized translation stage along the optical axis. This translation stage will allow phase diversity applications [16, 17].

The testbed also includes a pupil plane camera (CamP), a 4D AccuFiz interferometer for alignment and wavefront measurements, and convergent mirrors.

Combining all these components, the total wavefront error (WFE) in the testbed is 150nm RMS without the correction from the DMs. This enables the use of $\lambda/20$ surface error optics and an alignment tolerance of 100 to 500µm, depending on the optic.

C. Environment constraints

To limit air turbulence and dust on the optical components, which would degrade the contrast performance, HiCAT is located in a class 1000 clean room with temperate control in a 1°C range and humidity that is maintained under 40%. Furthermore, the testbed is on a floating table, which is on a platform independent from the rest of the building, to remove vibration effects. A box covers all the testbed to protect it from dust and particles.

In addition to these first protections, the deformable mirrors have stronger constraints, in particular about humidity (below 30%), which lead to the installation of temperature and humidity sensors and a complementary dry air system inside the box containing the optical bench.

This air supply may create unwanted turbulence effects in the bench box, that might make the wavefront more unstable and so high-contrast imaging implementation more challenging. This is why we plan to make this supply external by limiting the humidity in the entire room below 30%, which would minimize the turbulence inside the box.

D. Timeline and first results

The HiCAT testbed was fully aligned in Summer 2014, except for the three deformable mirrors (2 Boston-DMs and the Iris-AO segmented mirror) and the apodizer. This alignment resulted in a wavefront errors of 12±3nm RMS over an 18mm circular pupil, after passing through an optical train of 15 components. Fig. 2 shows the direct and coronagraphic images obtained at the end of the testbed after this alignment. The direct image corresponds to a nice Airy diffraction pattern, with seven visible rings. Furthermore, the coronagraphic image shows a lot of speckles, that result from the residual wavefront errors of the testbed, and was not optimized at that time since the FPM and the Lyot Stop were not optimally centered yet.

In 2015, the first DM was calibrated and integrated into the testbed, and replaced a flat mirror located in a pupil plane. After alignment of the DM, we obtained a wavefront error of 13±3nm RMS, which makes us hope for very good results after implementation of wavefront control.

Unfortunately, the first wavefront control tests could not be achieved, due to an instability issue, that is described in [18]. The resolution of this problem is currently on going, and once it will be solved, the wavefront control implementation will go on, leading to the installation of the second DM to apply also the ACAD method. Furthermore, the apodizer design studies is on-going and gives very promising results and an apodizer should be added to the optical bench.

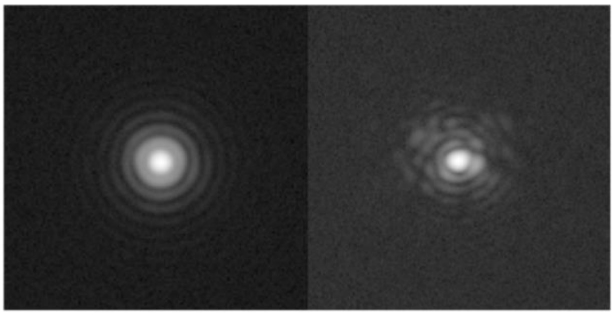

Fig. 2. Direct and coronagraphic PSF obtained at the end of the HiCAT testbed, in log scale, but not on the same scale. A 18mm circular pupil was used, combined with a 10mm Lyot Stop. The source gives a monochromatic light at λ=640nm.

III. SPECKLE NULLING SIMULATION TESTS:

In this section, after a short introduction to wavefront control, we describe a first method which does not need any estimation of the wavefront. It was implemented in simulation mode and gave first really promising results.

A. Introduction to wavefront control methods

Since Brown and Burrows set [19] the typical requirements in term of contrast for exoplanet detection, the theoretical feasibility of starlight subtraction in a so-called dark hole thanks to a DM has been proven [20]. This approach has been simplified with linearization of the equations to become the Speckle Nulling algorithm which has already several times been experimentally tested and has proven its efficiency and its robustness in broadband light [21, 22]. A first generalization of this method (Speckle Field Nulling), which is based on minimization of the speckle energy in all over the dark hole thanks to a Fast-Fourier-Transform-based (FFT) algorithm, has been developed [23]. In opposition to these estimation-free approaches, model-based techniques have been developed and implemented. They separate estimation and control for a faster correction, such as the Self-Coherent Camera (SCC) [24] and the COronagraphic Focal-plane waveFront Estimation for Exoplanet detection (COFFEE) [25] for the estimation, or the Electric Field Conjugation (EFC) [26, 27] and the Stroke Minimization [28], including even multiple DMs to enable symmetric correction in the dark hole (both amplitude and phase aberration correction). Another algorithm was developed by Baptiste Paul, the so-called Non-Linear Dark Hole, which does not make any linearization of the wavefront [29].

In this section, we describe in the first part the Speckle Nulling code that is applied in simulation mode in the case of a circular aperture and the results we obtain. In the second part, we add random tip-tilt vibrations in the pupil plane of our simulated system and study the influence of this perturbation on the results.

B. Simulation without perturbation

We wrote a code that is split in different parts, to separate the simulation-only sections from the sections common to the simulation mode and to the on-testbed mode. The simulation-only sections are equivalent on the testbed to an image acquisition and therefore contain a simulated Lyot coronagraph similar to the HiCAT configuration. A visual description of the code is given in Fig. 3.

The Speckle Nulling method does not uniformly correct the image in the all dark hole. It typically focuses on the correction of the n brightest speckles of the dark hole. For example, if we only want to correct for one single speckle, the Speckle Nulling method selects the brightest speckle of the dark hole and computes its intensity I and its position (u_x, u_y), according to the center of the PSF.

Since one speckle in the field is equivalent to a sine function of the wavefront surface in the pupil plane, we are looking for an equation of the unknown error phase in the pupil plane such as:

$$\phi = A \times \sin(\varphi_0 + 2\pi \times (f_x x + f_y y))$$

where A is the amplitude of the sine, φ_0 is the origin phase and f_x and f_y are the spatial frequencies of the phase and can easily be computed from the position (u_x, u_y) of the speckle.

Furthermore, to estimate the amplitude of the sine function, we add a calibration step before the correction. A known sine function is applied on the DM surface and we simulate the resulting image in the focal plane behind the coronagraph. This image has two symmetrical speckles, and we can get their intensity. According to this value and the amplitude of the sine command sent to the DM, we have a conversion factor from the DM command to the intensity of the image points.

$$A = C \times A_0 \times \sqrt{\frac{I}{I_0}}$$

where A is the calculated amplitude, A_0 is the amplitude of the calibration sine command, C is the conversion factor, I is the intensity of the speckle that has to be corrected, and I_0 is the intensity of the calibration speckle. The main problem is finding the spatial phase φ_0. As explained in Fig. 3, it is found by testing different possible spatial phases and selecting thanks to an interpolation the one that gives the best results on the corrected image.

We apply the procedure described before on a simulated coronagraph with a Lyot Stop size equal to 0.99 times the pupil size. In this case, since we are working on simulated data, we fix the DM size to 136 actuators, so 4 times larger than our real DM. The error phase is set as shown on Fig. 4 on the top left image and we just have access to the top right image, which is the input of the routine.

We can also observe the results that we obtain after applying the Speckle Nulling code with the best correction to the images. As we can see, the correction was very efficient: in this case, the value of the speckle changed from 0.6898 to 0.01247 and on the corrected image, no speckle is visible. If we look at Fig. 5, the absence of speckle

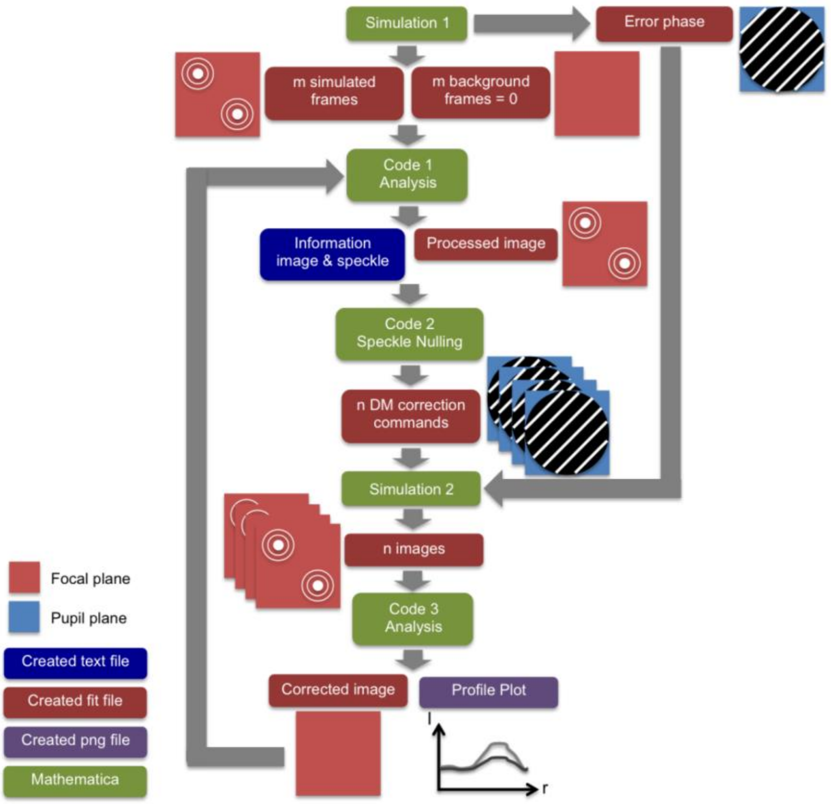

Fig. 3. Diagram of our Speckle Nulling code. The code has been written to work in two different modes: with simulated data or experimental images on the testbed. Simulations 1 and 2 are dedicated to the simulation mode only while Codes 1, 2 and 3 are common to the two modes. Simulation 1 sets up all the useful input for the rest of the procedure: an "unknown" phase error (here: a sine function), background frames and image plane frames obtained with a Lyot coronagraph. Code 1 computes the characteristics of the selected speckle (spatial frequency and amplitude) and takes the average background-subtracted image. Code 2 generates n DM commands to probe different spatial phases of the selected speckle. Simulation 2 computes the coronagraphic images in the presence of unknown phase for each of the n commands applied on the DM. Finally, Code 3 analyses these images to determine the phase and the corresponding DM command that leads to the best correction of the selected speckle.

on the corrected image also clearly appears.

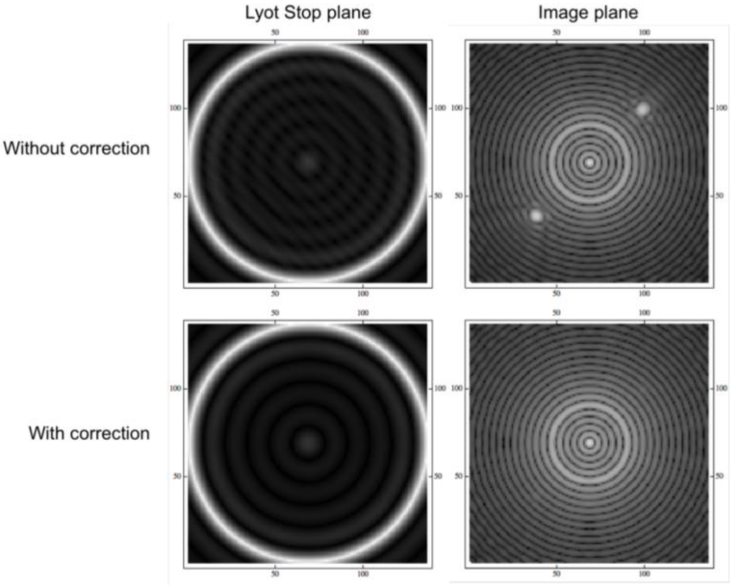

Fig. 4. First results obtained with the Speckle Nulling code with simulated images before and after correction of a pair of speckles (top and bottom). Left: Images in the relayed pupil plane of the coronagraph before application of the Lyot stop. Right: Coronagraphic images in the final image plane.

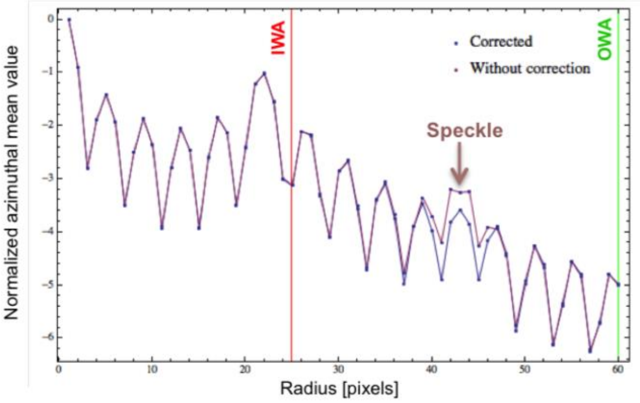

Fig. 5. Azimuthal averaged intensity profiles of the coronagraphic images in log scale for the initial image (purple) and the corrected image (blue) that are displayed in Fig. 4. The IWA and OWA of the controlled region are represented with vertical lines. The attenuation of the intensity is observed at the speckle location (44 pixels).

C. Simulation with perturbation

In this part, fake random vibration are added in the pupil plane before the coronagraph, that is equivalent of the DM plane.

To do so, we generate a vector of n random tip values and a vector of n random tilt values, in a certain range. We can then compute the n corresponding wavefronts in the DM plane and we add them to our phase error. After that, we can simulate the n images behind the coronagraph that are used as an input of the procedure. We apply random vibration before summing the input images and also before applying the correction phases tested on the DM. Except for these two extra steps, the code is applied similarly than in the previous case.

As shown on Fig. 6, the vibration effect is clearly visible both before and after correction. In average, the correction is still doable, the vibration does not prevent the code from working.

The main effects of the vibration are that we can obtain random results, sometimes really good and sometimes really bad, which is due to the fact that after correction, we take a single snapshot and the random tip-tilt can be small or important. Furthermore, the translation of the pattern appears on the azimuthal plot. Indeed, we observe both a translation of the rings and a smoothing of the values, as shown on Fig. 6.

The Fig. 7 indicates the performance depending on the vibration amplitude maximum range. For every maximum range, we apply the code 5 times and obtain a set of 5 speckle values after correction. We then look at the minimum obtained value, which corresponds to the best performance, the average value and the maximum value (worst correction). As shown on Fig. 8, the higher the instability amplitude is, the more random the results are, even if in every case we can still obtain very good results (the minimum value is quite constant).

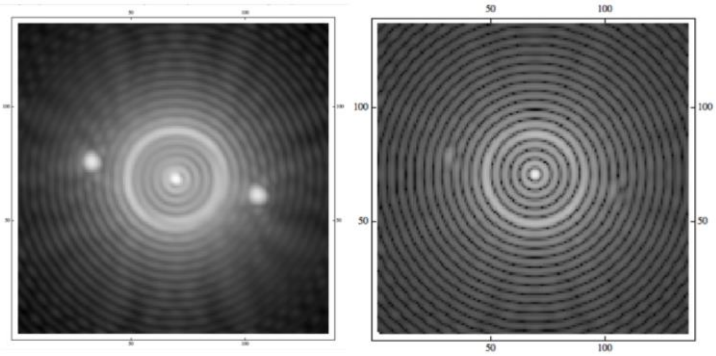

Fig. 6. Coronagraphic images without and with correction, in presence of vibration. Left: Averaged image of 10 frames with random tip and tilt within the amplitude range [-0:01λ, +0:01λ]. Right: one single snapshot after correction, with a similar random tip-tilt vibration. In both images, the tip and tilt aberrations are visible with the asymmetry of the diffraction rings that are produced by the Lyot coronagraph. As the correction is applied at a certain position, it does not necessarily correspond to the right speckle location since a tip-tilt is added. The correction is therefore less efficient than in the case we work without vibration.

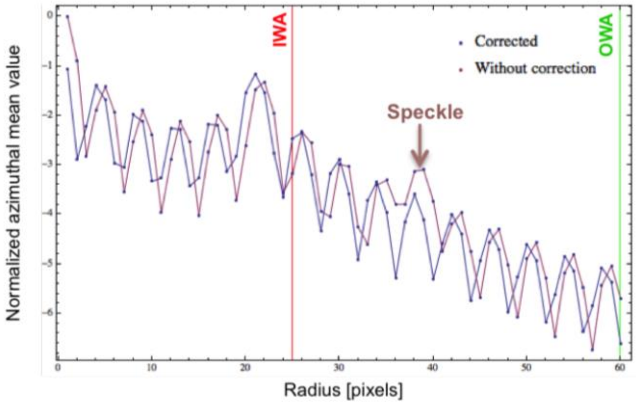

Fig. 7. Azimuthal averaged intensity profiles of the simulated coronagraphic images in log scale for the non-corrected image (purple) and the corrected image (blue) that are displayed in Fig. 6. The IWA and OWA of the controlled region are represented with vertical lines. A shift of the diffraction rings is observed between the two cases. The attenuation of the speckle at its location is less important than the reduction observed in the absence of vibration in Fig. 5.

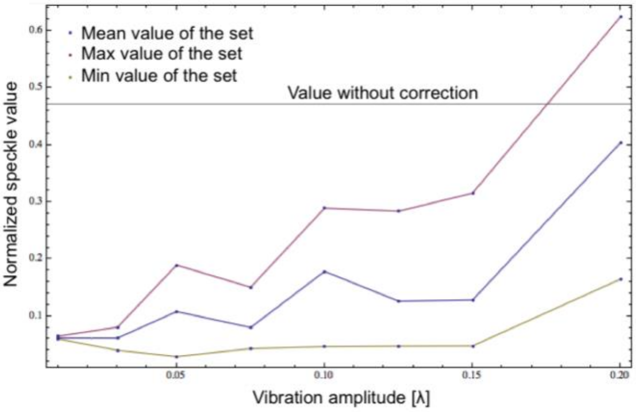

Fig. 8. Intensity of the speckle after correction as a function of the maximum vibration amplitude. For every maximum range, we apply the code 5 times and obtain a set of 5 speckle values after correction. From this analysis, we retrieve the minimum obtained value, which corresponds to the best performance (yellow curve), the average value (blue curve) and the maximum value that corresponds to the worst correction (pink curve).

IV. CONCLUSIONS AND PERSPECTIVES:

The HiCAT testbed will enable high-contrast imaging studies for telescopes with segmented apertures, spiders and/or central obstruction. It is designed as a coronagraph completed with two deformable mirrors to perform wavefront sensing and wavefront control and address both phase and amplitude aberrations.

In parallel to this experimental study, we coded a preliminary version of a Speckle Nulling code that gives good results in simulation mode, even in presence of pupil plane instability. Without vibration, a given speckle is fully removed after correction. In presence of vibration, we obtain a reduction of the speckle intensity in almost every case.

However, this method had some drawbacks, such as the computing speed. Indeed, since Specle Nulling only corrects for one speckle at once in the dark hole, it has to be applied many times in a row to correct for speckles in the entire dark hole. This is why, after this first test, we want to focus on other methods, such as the ones that have been described in section III.A. The objective is comparing the performance in contrast of this different methods, but also their requirements and their robustness to realistic space-like environment conditions, such as jitter. After this study, amethod should be selected to be implemented on the HiCAT testbed for further studies.

REFERENCES

[1] D. Spergel, N. Gehrels, C. Baltay, D. Bennett, J. Breckinridge, et al., *Wide-Field InfrarRed Survey Telescope-Astrophysics Focused Telescope Assets WFIRST-AFTA 2015 Report*, ArXiv e-prints, March 2015.

[2] M. Postman, T. Brown, K. Sembach, M. Giavalisco, W. Traub, et al., "Advanced Technology Large-Aperture Space Telescope: science drivers and technology developments", *Optical Engineering*, 51, 011007, January 2012.

[3] L. D. Feinberg, A. Jones, G. Mosier, N. Rioux, D. Redding, and M. Kienlen, "A Cost-effective and Serviceable ATLAST 9.2m Telescope Architecture", *SPIE 9143*, 1-11, 2014.

[4] J. Dalcanton, S. Seager, S. Aigrain, S. Battel, N. Brandt, et al., "From Cosmic Birth to Living Earths: The Future of UVOIR Space Astronomy", ArXiv e-prints, July 2015.

[5] M. N'Diaye, L. Pueyo, and R. Soummer, "Apodized Pupil Lyot Coronagraphs for Arbitrary Apertures. IV. Reduced Inner Working Angle and Increased Robustness to Low-order Aberrations", *Astrophysical Journal* 799, 225, February 2015.

[6] M. N'Diaye, R. Soummer, L. Pueyo, A. Carlotti, C. Stark, and M. D. Perrin, "Apodized Pupil Lyot Coronagraphs for Arbitrary Apertures. V. Hybrid Shaped Pupil Designs for Imaging Earth-like planets with Future Space Observatories", *Astrophysical Journal* 818, 163, February 2016.

[7] M. N'Diaye, J. Mazoyer, E. Choquet, L. Pueyo, M. D. Perrin, et al., "High-contrast imager for complex aperture telescopes (HiCAT): 3. First lab results with wavefront control", *SPIE*, 9605, 12, September 2015.

[8] L. Pueyo and C. Norman, "High-contrast Imaging with an Arbitrary Aperture: Active Compensation of Aperture Discontinuities", *Astrophysical Journal* 769, 102, June 2013.

[9] J. Mazoyer, L. Pueyo, C. Norman, M. N'Diaye, and R. Soummer, "Correcting for the effects of pupil discontinuities with the ACAD method", *SPIE* 9904, 2016.

[10] J. Mazoyer, L. Pueyo, C. Norman, M. N'Diaye, R. P. van der Marel, and R. Soummer, "Active compensation of aperture discontinuities for WFIRST-AFTA: analytical and numerical comparison of propagation methods and preliminary results with a WFIRST-AFTA-like pupil", *Journal of Astronomical Telescopes, Instruments, and Systems 2*, March 2016.

[11] M. N'Diaye, E. Choquet, L. Pueyo, E. Elliot, M. D. Perrin, et al., "High-contrast imager for Complex Aperture Telescopes (HiCAT): 1. Testbed design", *SPIE*, 8864, September 2013.

[12] M. N'Diaye, E. Choquet, S. Egron, L. Pueyo, L. Leboulleux, et al., "High-contrast Imager for Complex Aperture Telescopes (HICAT): II. Design overview and first light results", *SPIE*, 9143, 27, August 2014.

[13] J. K. Wallace, S. Rao, R. M. Jensen-Clem, and G. Serabyn, "Phase-shifting Zernike interferometer wavefront sensor", *SPIE*, 8126, September 2011.

[14] M. N'Diaye, K. Dohlen, T. Fusco, K. El Hadi, R. Soummer, et al., "Lab results of the circular phase mask concepts for high-contrast imaging of exoplanets", *SPIE*, 8450, September 2012.

[15] M. N'Diaye, K. Dohlen, T. Fusco, and B. Paul, "Calibration of quasi-static aberrations in exoplanet direct-imaging instruments with a Zernike phase-mask sensor", *Astron. & Astrophys.*, 555, A94, July 2013.

[16] B. H. Dean and C. W. Bowers, "Diversity selection for phase-diverse phase retrieval", *Journal of the Optical Society of America* A 20, pp. 1490-1504, August 2003.

[17] J.-F. Sauvage, L. Mugnier, B. Paul, and R. Villecroze, "Coronagraphic phase diversity: a simple focal plane sensor for high-contrast imaging", *Optics Letters* 37, p. 4808, December 2012.

[18] L. Leboulleux, M. N'Diaye, A. J. Eldorado Riggs, S. Egron, J. Mazoyer, "High-contrast imager for Complex Aperture Telescopes (HiCAT). 4. Status and wavefront control development", *SPIE*, July 2016.

[19] R. A. Brown and C. J. Burrows, "On the feasibility of detecting extrasolar planets by reflected starlight using the Hubble Space Telescope", *Icarus* 87, 484-497, October 1990.

[20] F. Malbet, J. W. Yu, M. and Shao, "High-Dynamic-Range Imaging Using a Deformable Mirror for Space Coronography", 107, 386, April 1995.

[21] J. T. Trauger, C. Burrows, B. Gordon, J. J. Green, A. E. Lowman, et al., "Coronagraph contrast demonstrations with the high-contrast imaging testbed", *SPIE* 5487, 1330-1336, October 2004.

[22] R. Belikov, A. Give'on, J. T. Trauger, M. Carr, N. J. Kasdin, et al., "Toward 10^{10} contrast for terrestrial exoplanet detection: demonstration of wavefront correction in a shaped-pupil coronagraph", *SPIE* 6265, 62651, June 2006.

[23] P. J. Bordé and W. A. Traub, "High-Contrast Imaging from Space: Speckle Nulling in a Low-Aberration Regime", *ApJ* 638, 488-498, February 2006.

[24] J. Mazoyer, P. Baudoz, R. Galicher, and G. Rousset, "High-contrast imaging in polychromatic light with the self-coherent camera", *AAJ* 564, L1, April 2014.

[25] B. Paul, J.-F. Sauvage, L. M. Mugnier, K. Dohlen, T. Fusco, et al., "Simultaneous phase and amplitude retrieval with COFFEE: from theory to laboratory results", *SPIE* 9147, 91479O, July 2014.

[26] A. J. E. Riggs, N. J. Kasdin, and T. D. Groff, "Recursive starlight and bias estimation for high-contrast imaging with an extended Kalman filter", *JATIS* 2(1), 011017, 2016.

[27] A. Give'on, B. D. Kern, and S. Shaklan, "Pair-wise, deformable mirror, image plane-based diversity electric field estimation for high contrast coronagraphy", *SPIE* 8151, 815110, October 2011.

[28] L. Pueyo, J. Kay, N. J. Kasdin, T. D. Groff, M. McElwain, et al., "Optimal dark hole generation via two deformable mirrors with stroke minimization", *Appl. Opt.* 48, 6296-6312, November 2009.

[29] B. Paul, "Mesure de front d'onde post-coronographique à haute précision pour l'imagerie à haut contraste : application sol et espace", PhD thesis, September 2014.